ACSNANO

www.acsnano.org

ARTICLE

Controlling the Spatial and Momentum Distributions of Plasmonic Carriers: Volume *vs* Surface Effects

Jacob Pettine, Sean M. Meyer, Fabio Medeghini, Catherine J. Murphy,* and David J. Nesbitt*

Cite This: *ACS Nano* 2021, 15, 1566–1578

Read Online

ACCESS | Metrics & More | Article Recommendations | Supporting Information

ABSTRACT: **Spatial and momentum distributions of excited charge carriers in nanoplasmonic systems depend sensitively on optical excitation parameters and nanoscale geometry, which therefore control the efficiency and functionality of plasmon-enhanced catalysts, photovoltaics, and nanocathodes. Growing appreciation over the past decade for the different roles of volume- *vs* surface-mediated excitation in such systems has underscored the need for explicit separation and quantification of these pathways. Toward these ends, we utilize angle-resolved photoelectron velocity map imaging to distinguish these processes in gold nanorods of different aspect ratios down to the spherical limit. Despite coupling to the longitudinal surface plasmon, we find that resonantly excited nanorods always exhibit transverse (sideways) multiphoton photoemission distributions due to photoexcitation within volume field enhancement regions rather than at the tip hot spots. This behavior is accurately reproduced *via* ballistic Monte Carlo modeling, establishing that volume-excited electrons primarily escape through the nanorod sides. Furthermore, we demonstrate optical control over the photoelectron angular distributions *via* a screening-induced transition from volume (transverse/side) to surface (longitudinal/tip) photoemission with red detuning of the excitation laser. Frequency-dependent cross sections are separately quantified for these mechanisms by comparison with theoretical calculations, combining volume and surface velocity-resolved photoemission modeling. Based on these results, we identify nanomaterial-specific contributions to the photoemission cross sections and offer general nanoplasmonic design principles for controlling photoexcitation/emission distributions *via* geometry- and frequency-dependent tuning of the volume *vs* surface fields.**

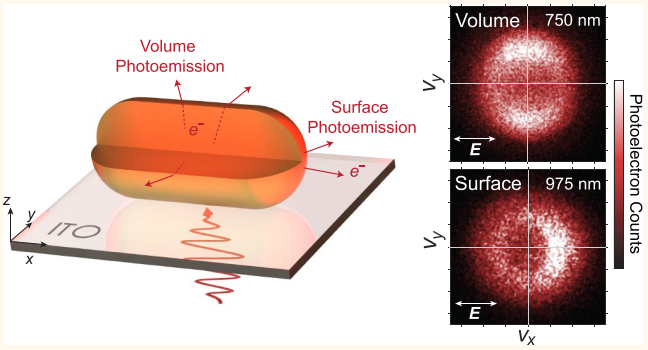

KEYWORDS: *velocity map imaging, angle-resolved photoemission, gold nanorods, Monte Carlo, single particle, ultrafast, multiphoton photoemission*

Electron emission studies of solids under ultraviolet (UV) or X-ray irradiation have been essential to fundamental developments in quantum mechanics and insights into electronic structure and physical properties of materials.[1] Of particular recent interest has been the elucidation of photoemission dynamics from nanoscale materials, with special emphasis on plasmonic metal nanoparticles and nanostructures.[2−9] The presence of low-energy visible and near-infrared (IR) plasmon resonances and the extraordinary optical field concentration in these systems has revitalized the nearly century-old problem of distinguishing between (i) electron excitation throughout the material volume, followed by ballistic transport and escape, and (ii) excitation and emission directly from the surface.[10−15] A detailed understanding of these mechanisms in nanoscale systems will provide additional opportunities for designing and dynamically controlling plasmonic charge carrier distributions in emerging photocatalytic,[14,16,17] photovoltaic,[13,18] and nanocathode[7,8,19] applications.

At the heart of this issue is the negligible linear momenta of incoming photons compared with outgoing electrons. Momentum conservation thus demands electron scattering with a massive third body during photoexcitation and emission. Volume-mediated excitation is dominated by scattering with

Received: October 29, 2020
Accepted: December 31, 2020
Published: January 11, 2021

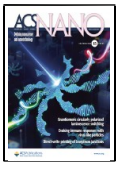

https://dx.doi.org/10.1021/acsnano.0c09045
ACS Nano 2021, 15, 1566–1578

the periodic lattice potential when such a transition is energetically allowed, but visible/near-IR excitation energies are often below the relevant interband energies in noble metals, and intraband excitation must instead proceed *via* scattering with phonons, defects, impurities, or other electrons.[20,21] The local *n*-photon volume excitation density depends on the total magnitude of the electric field, $|E(\mathbf{r})|^{2n}$. By contrast, surface photoexcitation/emission arises due to the translational symmetry breaking at the metal−environment interface and thus involves scattering with the surface potential barrier, including contributions from surface electromagnetic field variations, localized surface states, and the evanescent external decay of internally delocalized Bloch wave functions.[11,20,22] In nanoplasmonic systems, the few-nanometer exponential decay of external electric fields can contain sufficiently large wavevector components to act as a prominent source of momentum.[23] Unlike volume excitation, the local *n*-photon surface-mediated excitation rate depends only on the surface-normal component of the electric field, $|E_{\perp}(\mathbf{r})|^{2n}$, which has been exploited to distinguish volume *vs* surface photoemission contributions from metal films *via* s- and p-polarized electromagnetic fields.[24−26] Further details on the volume *vs* surface photoemission paradigm and potential ambiguities in this dichotomy can be found in SI Section 1, along with a discussion of possible coherent *vs* incoherent multiphoton photoexcitation pathways and implications thereof in SI Section 2.

Localized surface plasmonic field enhancement hot spots are often highly spatially distinct from volume field-enhanced regions, yielding correspondingly distinct spatial and angular photoexcited carrier distributions[27,28] and providing a relatively unexplored optical control degree of freedom that can be harnessed for plasmonic devices. Plasmonic hot carrier catalysts, for instance, already exhibit high reaction efficiencies and product specificity compared with thermally activated processes,[16,17] as demonstrated *via* CO_2 conversion[29] and H_2O splitting[14,30] for solar fuel production. However, further enhancements in catalytic activity and device functionality can be achieved by controlling the plasmonic carrier spatial and momentum degrees of freedom to complement anisotropic coatings[18,30−32] and even introduce nanoscale site selectivity,[6,33] with similar opportunities in broadband photodetection[34,35] and solar energy conversion.[36,37] Plasmonic nanoparticles and nanostructured arrays also serve as bright photocathode emitters,[3,38] with possibilities for optically controlled current directionality[8] in terahertz nanoelectronics[19] and femtosecond electron imaging[39,40] applications. While internal electron emission at metal−molecule[14] or metal−semiconductor[13,30,31] interfaces is often classified by either "direct" excitation at the surface or "indirect" transfer following volume excitation,[16,17,21,37,41] these mechanisms closely parallel surface *vs* volume photoemission for metal−vacuum interfaces. A deeper understanding of volume and surface effects in nanoplasmonic systems is therefore essential to a variety of applications, regardless of the collection medium.

The primary focus of the present work is to distinguish volume *vs* surface photoemission pathways in plasmonic nanoparticles by the distinctly different photoelectron momentum distributions. We begin with the observation that laser excitation of longitudinal dipolar surface plasmon resonances (SPRs) in gold nanorods results in transverse (orthogonal) multiphoton photoemission (*n*PPE) through the cylindrical sides, which is shown to be due to volume excitation. We then demonstrate a previously unexplored transition from volume (transverse/side) to surface (longitudinal/tip) *n*PPE that occurs with red detuning of the excitation laser, resulting from the more effective metallic screening of internal electric fields at lower frequencies. A combination of three-dimensional (3D) velocity-resolved semiclassical volume and quantum surface *n*PPE modeling reproduces all of these effects and enables quantitative characterization of the photoemission cross sections. Most importantly, we demonstrate that the relative volume *vs* surface *n*PPE contributions depend primarily on plasmonic field enhancement distributions, which are readily simulated *via* classical numerical (*e.g.*, finite element or finite difference) methods for solving Maxwell's equations. Although measurements are performed in the 2-, 3-, and 4-photon regimes with visible and near-IR excitation to overcome the ∼4.3 eV gold nanorod work functions, much of the analysis is general with respect to process order and is therefore expected to remain valid down to the linear regime for single-photon applications. These results provide general design principles for (i) engineering nanoplasmonic geometries to promote volume or surface processes and (ii) dynamically controlling the corresponding photocurrents *via* optical frequency- and/or polarization-dependent plasmonic field distributions.

RESULTS AND DISCUSSION

Transverse Volume Photoemission from Gold Nanorods. Strong electric near-field enhancements are generated at the tips of gold nanorods where conduction electrons pile up during dipolar longitudinal localized SPR oscillations. At the same time, appreciable field enhancements are also generated within the metal volume. The surface-normal fields concentrated at the nanorod tips are spatially well separated from the volume fields, which are concentrated near the center of the cylindrical body, leading to distinct surface *vs* volume photoexcitation/emission pathways. These are illustrated in Figure 1a, along with the scanning photoelectron imaging microscopy (SPIM) experimental configuration (Methods). Different photoemission angular distributions are expected for the two mechanisms,[27] depending upon the nanoparticle geometry and the electric near-field distribution of the excited plasmon mode, which provides a direct means of identifying the source of plasmonic carriers (electrons and their corresponding holes) *via* single-particle, angle-resolved photoelectron velocity mapping.

Photoemission spectra are shown in Figure 1b for nanorods of similar diameter, $D = 21 \pm 4$ nm (Figure S1), but different lengths and thus aspect ratios (L/D), illustrating the anticipated linear increase of the dipolar SPR wavelength with nanorod aspect ratio for $L/D \gtrsim 2$, as summarized in Figure S2.[42,43] Only longitudinal SPRs are investigated, as the transverse nanorod SPR excitation is much weaker and does not reveal additional insights for the present purposes. Additionally, while only dipolar modes are excited in the present size and frequency range, higher-order multipolar SPR modes are fully accounted for in the finite element simulations (Methods). For the gold nanorod work function around 4.25 eV, electrons must absorb multiple photons to overcome the surface potential barrier, with nanorod resonances ranging from 950 nm (1.3 eV photon energy, $n = 4$ photons) at $L/D = 5$ down to the spherical limit of 540 nm (2.3 eV photon energy, $n = 2$ photons) at $L/D = 1$. Measurements of the photoemission dependence on linear laser polarization (angle

https://dx.doi.org/10.1021/acsnano.0c09045
ACS Nano 2021, 15, 1566−1578

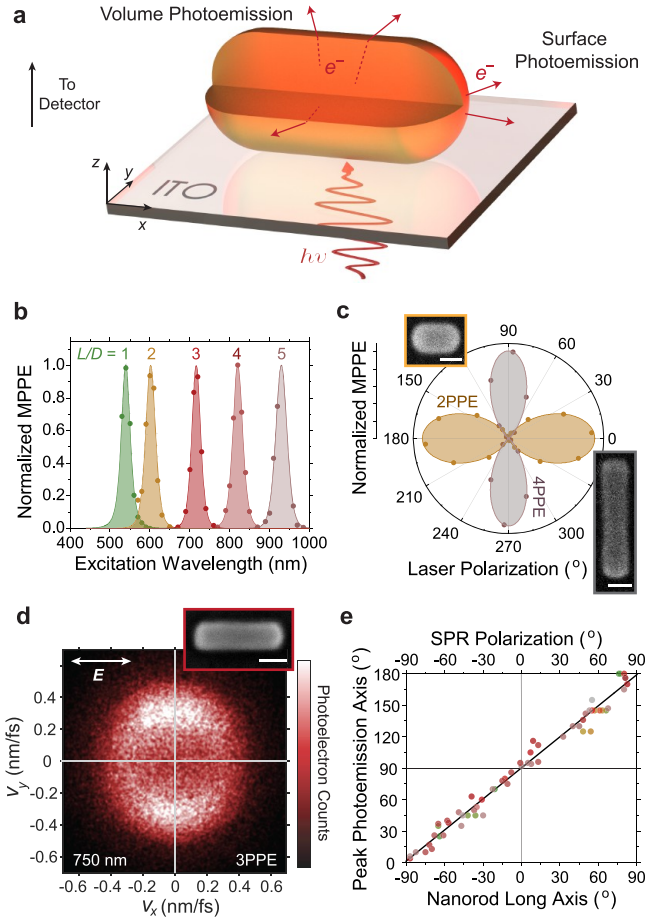

Figure 1. Characterization of nanorod surface plasmon resonance photoemission properties. (a) Configuration of SPIM experiments, illustrating volume and surface emission from an illuminated gold nanorod (with a cutaway showing the volume excitation). (b) Multiphoton photoemission spectra, measured for nanorods of various aspect ratios, fit to nonlinear Lorentzian profiles. (c) Signal dependence on linear laser polarization in the azimuthal (xy) plane, fit to $\cos^{2n}(\theta - \theta_{rod})$ and shown with scanning electron micrographs of the correlated nanorods (L/D = 1.5, 2PPE and L/D = 4.5, 4PPE), where laser polarization $\theta = 0°$ is along the x axis. (d) Photoelectron velocity map collected at the longitudinal resonance of the correlated L/D = 3.2 nanorod in the inset, exhibiting transverse photoemission. (e) Summary of photoemission directionality for all nanorods of various aspect ratios and spatial orientations, with transverse distributions observed in every case. Data colors (here and elsewhere) are mapped to the corresponding wavelength. Scale bars: 20 nm.

θ) in the azimuthal plane (Figure 1c) show clearly defined longitudinal resonances along the long nanorod axes, noticeably narrowing in the 4-photon regime ($L/D \sim 4.5$) relative to the 2-photon regime ($L/D \sim 1.5$) due to the nPPE $\propto E^{2n}$ $\cos^{2n}(\theta - \theta_{rod})$ dependence of the field projection along the nanorod axis. Pulse durations around 150 fs (Methods), pulse peak intensities of 10^8 W cm^{-2} (SI Section 4), and calculated nanorod extinction cross sections around 10^{-10} cm^{-2} lead to the excitation of nearly 10^4 plasmons/pulse, which is much larger than the 2−4 quanta absorbed in nPPE (one nPPE event every $\sim 10^5$ pulses, with a 75 MHz laser repetition rate), thus justifying a classical treatment of the plasmonic fields.

While longitudinal electron emission outward from the highly field-enhanced nanorod tips has been observed in the strong-field tunneling[7,44] and transitional regimes,[5] here we find that weak-field nPPE is predominantly transverse (orthogonal) to the resonantly excited longitudinal nanorod axis, as demonstrated in Figure 1d. In other words, electrons are evidently emitted from the sides rather than the tips of the nanorods. We observe this transverse photoemission for every nanorod investigated (Figure 1e), irrespective of aspect ratio (L/D = 1.5−5), surface ligands (Figure S5), size (D = 10−40 nm, Figure S5), or corresponding size-dependent differences in faceting.[45] Electron thermalization effects during the pulse duration are accounted for *via* two-temperature modeling,[46] as discussed in detail in the SI Section 4, where intensity-dependent studies also demonstrate negligible thermionic or thermally assisted emission effects. Furthermore, measurements with even shorter (dispersion-compensated) 40−50 fs pulses yield the same transverse nPPE distributions (Methods).

As the surface-normal field ($|E_\perp|^{2n}$ for nPPE) is negligible on the nanorod sides under longitudinal dipolar SPR excitation, the transverse photoemission distributions provide a strong initial indication that volume-mediated nPPE is dominant for resonantly excited nanorods. Electrons excited throughout the nanorod volume are thus expected to escape ballistically from the cylindrical body with a predominantly transverse distribution and from the hemispherical tips with a nearly isotropic distribution. As a starting point, assuming uniform excitation throughout the nanorod volume and a short inelastic mean-free path ($\lambda_{inel} \ll D$), the relative side *vs* tip contributions can be approximately estimated by the ratio of corresponding surface areas, which works out to be $S_{side}/S_{tip} = L/D - 1$. We therefore expect the photoemission distribution to become isotropic as $L/D \to 1$ ($S_{side} \ll S_{tip}$) or to become increasingly dominated by transverse contributions as $L/D \to \infty$ ($S_{side} \gg S_{tip}$).

To show definitively that the photoemitted electrons primarily originate within the volume of the resonantly excited nanorods, photoemission distributions are measured as a function of nanorod aspect ratio. As anticipated, the two-dimensional (2D) velocity maps in Figure 2a demonstrate that the photoemission angular distributions become more isotropic with decreasing aspect ratio and completely isotropic in the spherical limit. The radially integrated angular distributions in Figure 2c can be characterized by an angular contrast, AC, defined as

$$\mathrm{AC} = \frac{\langle \parallel \text{ counts} \rangle - \langle \perp \text{ counts} \rangle}{\langle \parallel \text{ counts} \rangle + \langle \perp \text{ counts} \rangle} \quad (1)$$

where the brackets denote averaging (within ±2°) over the two longitudinal (0° and 180°) and transverse (90° and 270°) directions on the 2D velocity maps. This definition of the angular contrast provides a model-independent metric of how transverse (AC → −1) or longitudinal (AC → 1) a given distribution is. Angular contrast values are summarized as a function of aspect ratio in Figure 2e, where AC clearly becomes more negative (transverse) as the nanorod aspect ratio increases and goes to zero in the isotropic spherical limit, as expected for the volume photoemission mechanism. The resonant excitation frequency primarily influences the radial distributions, with little impact on the angular distributions (SI Section 6), such that the AC trend in Figure 2e is due to the varying nanorod geometry and the corresponding photoexcitation spatial and momentum distributions. Note that the

https://dx.doi.org/10.1021/acsnano.0c09045
ACS Nano 2021, 15, 1566−1578

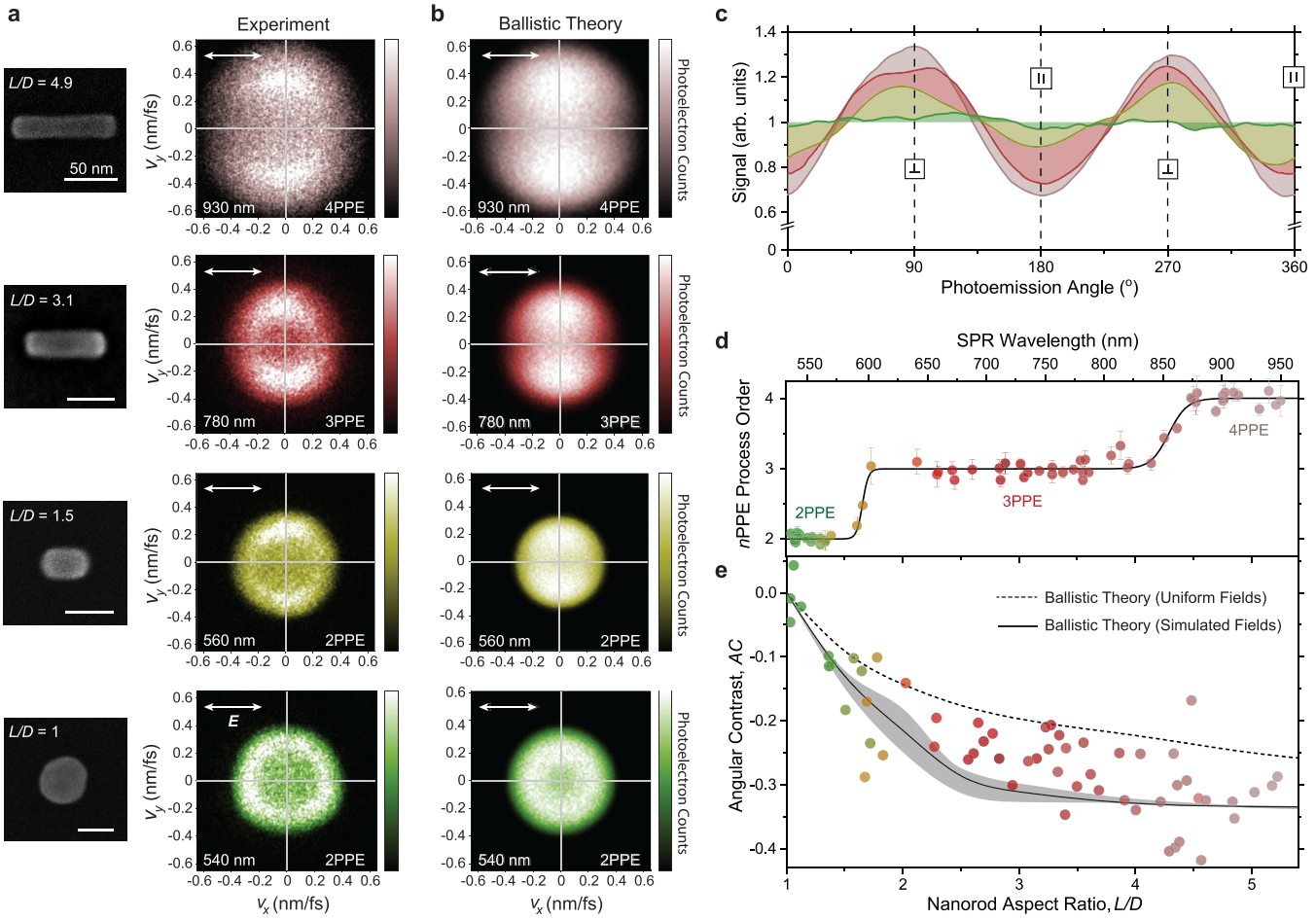

Figure 2. Volume photoemission distributions as a function of aspect ratio. (a) Correlated electron micrographs and velocity maps for a series of nanorods excited at their longitudinal SPRs, down to the spherical limit. Nanospheres of larger D = 70 nm are studied compared with nanorods (D = 20 nm) for sufficient signal levels, but this is neither expected nor observed to affect their photoemission properties. Scale bars: 50 nm. (b) Velocity distributions for the same nanorods as in (a), modeled using the ballistic (three-step) Monte Carlo theory. (c) Radially integrated angular distributions from the velocity maps in (a) with transverse (⊥) and longitudinal (||) directions indicated and 0° along the x (v_x) polarization axis. (d) Process order summary of n-photon photoemission measured *via* power-law intensity-dependent fits (also see Figure S3; error bars are standard errors of the fits) for all investigated nanorods under longitudinal SPR excitation, shown with overall sigmoidal fits. The SPR wavelength axis is linearly mapped (except around L/D = 1) to the aspect ratio (Figure S2). (e) Photoemission angular contrast of all investigated nanorods for longitudinal SPR excitation, becoming more negative (transverse) with increasing aspect ratio and isotropic in the spherical limit. Ballistic Monte Carlo theory curves shown for uniform and nonuniform (finite element simulated) internal fields. The error bounds shown for the simulated fields case assume an inelastic mean-free path between 7 nm (top) and 5 nm (bottom), with the primary curve calculated at 6 nm.

angular contrast, AC, and the photoemission mechanisms described herein are not to be confused with molecular photoionization and the corresponding anisotropy parameter.[47]

A summary of nonlinear process order, n (where nPPE ∝ I_0^n), from intensity-dependent measurements performed on resonance for each nanorod studied (Figure S3) is shown in Figure 2d. The results show a clear sequential transition from n = 2 up to n = 4 with increasing SPR wavelength and linearly correlated increasing aspect ratio (Figure 1b and Figure S2). The well-defined integer process orders and transitions verify that the present studies are performed in the perturbative nPPE regime rather than the optical field emission[38,48] or thermionic regimes (see SI Section 4 for an extended discussion). Non-integer process orders in the transition regions arise naturally in the power law fits and reflect the weighted sum of two contributing process orders (SI Section 4).[8] No sudden changes in photoemission angular distributions or corresponding angular contrast values are observed in the transition regions between process orders, and the photoemission physics is qualitatively the same at all nonlinear orders studied herein, just with a different total excitation energy ($n\hbar\omega$), corresponding nonlinear absorption cross sections, and more spatially diffuse E^2 field distributions compared with E^{2n}. We thus anticipate that the present observations can be extrapolated from the multiphoton regimes down to the linear regime for systems with lower emission barriers, including metal−semiconductor and metal−molecule junctions.

It is interesting to briefly highlight that L/D = 5 nanorods resonant in the 4PPE regime are approximately 5-fold brighter than L/D = 3 nanorods resonant in the 3PPE regime, which are themselves approximately 5-fold brighter than nanospheres resonant in the 2PPE regime. This can be seen in the summary of resonant nPPE cross sections in Figure S2 for $I_0 \approx 5 \times 10^7$ W cm^{-2} input intensities. Thus, despite the higher orders of

https://dx.doi.org/10.1021/acsnano.0c09045
ACS Nano 2021, 15, 1566−1578

perturbation and stronger screening (see General Design Principles), the geometrical effects of stronger internal plasmonic fields and larger excitation volumes for longer rods win out. Nevertheless, for a particular particle geometry, the photoemission rate decreases by multiple orders of magnitude with increasing process order (even neglecting the effect of detuning from resonance).[49]

To understand the volume *n*PPE distributions in further detail, we implement a Monte Carlo method within the ballistic, three-step photoemission model.[50] In this model, electrons are first excited to randomly selected vector momenta (approximating isotropic phonon-mediated multiphoton excitation) with *n*-photon Fermi–Dirac weighting, from points selected randomly throughout the nanorod volume. The volume element selection probability is weighted by the nonlinear internal field enhancement ($|E/E_0|^{2n}$) determined *via* electrodynamic finite element simulations with the ligands and substrate accounted for (Methods). The calculated pulse-averaged electron temperature of 1000 K (SI Section 4) is utilized for the excited Fermi–Dirac distribution to account for minor effects of electron heating during the pulse duration. Excited electrons then travel ballistically over some distance (d) to the surface with an exponential survival probability for inelastic hot–cold electron–electron scattering, $\propto e^{-d/\lambda_{inel}}$. The inelastic mean-free path, $\lambda_{inel} \approx 5$ nm,[51,52] is approximately constant over the narrow threshold energy range of interest (~4.5–6 eV above the Fermi level), and we account for the possibility of the nascent photoexcited electrons surviving a single inelastic scattering event with sufficient momentum to subsequently escape, although the contribution of these partially thermalized electrons is found to be negligible. Finally, electrons that reach the surface with sufficient surface-normal momentum to overcome the potential barrier escape into the surrounding medium with a quantum transmission probability (SI Section 6).

Refraction at the surface barrier and escape cone effects due to perpendicular momentum loss and parallel momentum conservation are fully accounted for in the 3D spatially and velocity resolved calculations. Trajectories following internal surface reflection could also be readily incorporated into the modeling and may be relevant for particle dimensions similar to or less than the inelastic mean-free path.[53,54] However, these trajectories are safely neglected here, as λ_{inel} is much smaller than the particle dimensions and internally surface-reflected electrons will have negligible probability of reaching another surface with sufficient energy to escape. While direct analytical integration methods have been used to investigate three-step volume photoemission from certain high-symmetry geometries,[53,55] the Monte Carlo method provides a computationally efficient means of integrating over all photoexcited electron trajectories for arbitrary nanoparticle geometries.[6,54,56] Further details of the ballistic Monte Carlo method are described in SI Section 6.

The calculated Monte Carlo velocity maps in Figure 2b and angular contrasts in Figure 2e accurately reproduce the experimental angular distributions, with a small discrepancy between the experimental and calculated angular contrast values due to minor surface photoemission contributions on resonance, as examined in the next section. Although the measured nanorod work function (4.25 ± 0.1 eV) is utilized in the calculations for an accurate Fermi edge, the overall radial distributions are evidently not reproduced as well as the angular distributions. This can be attributed to our approximation of (i) constant joint density of states and (ii) energy-independent excitation matrix elements utilized in the modeling. For detailed investigations of the radial distributions, *ab initio* treatments of the band structure and multiphoton excitation channels could also be incorporated.[57]

Frequency-Controlled Volume *vs* Surface Photoemission. For further insight into the roles of both volume and surface photoemission processes, we simulate the electric near-field distributions as a function of excitation frequency (and thus detuning from SPR) in Figure 3a. Unlike the well-known uniform internal fields for ellipsoids,[58] internal fields for nanorods are stronger near the center due to a more uniform

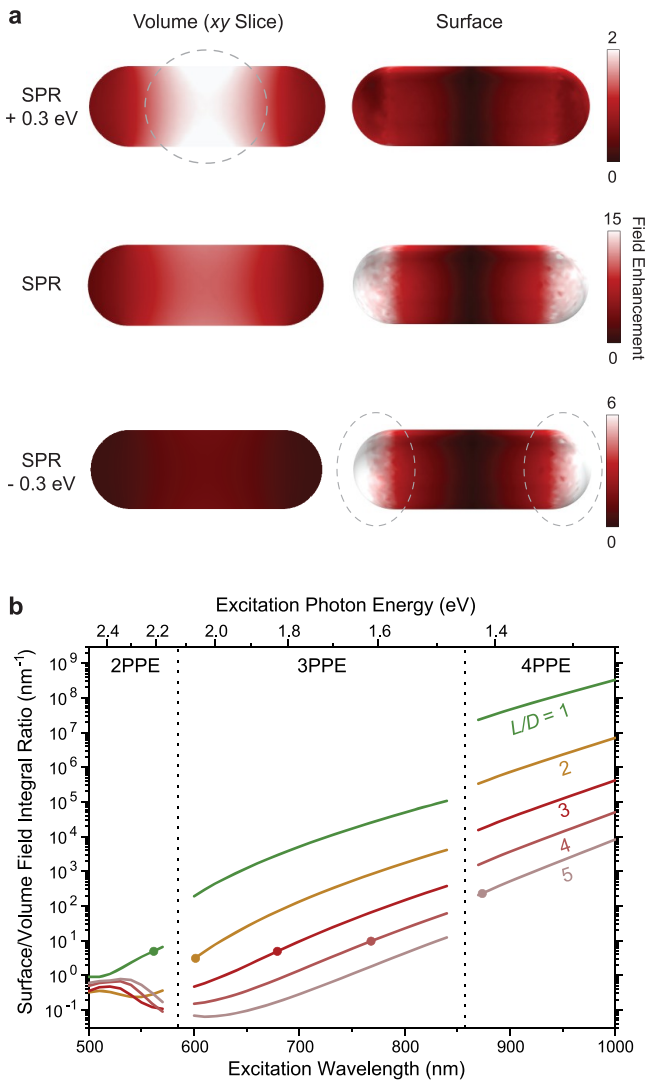

Figure 3. Finite element simulations of volume and surface plasmonic field enhancements. (a) Volume ($|E/E_0|$) and surface-normal ($|E_\perp/E_0|$) field enhancement maps for an $L/D = 3$ nanorod, viewed in the *xy* plane (ligand layer and ITO substrate accounted for but not shown; see Methods). Volume fields are dominant at higher excitation energies (*e.g.*, SPR + 0.3 eV), while surface fields are dominant at lower excitation energies (*e.g.*, SPR − 0.3 eV). (b) Ratio of the nonlinear surface field integral (as in eq 3a) to the nonlinear volume field integral (as in eq 3b) for a series of nanorod aspect ratios across the $n = 2–4$ spectral regions. The point on each curve indicates the calculated surface plasmon resonance wavelength. The fluctuations in the 2PPE regime are primarily due to the onset of 5d-band absorption and dispersion.

https://dx.doi.org/10.1021/acsnano.0c09045
ACS Nano 2021, 15, 1566–1578

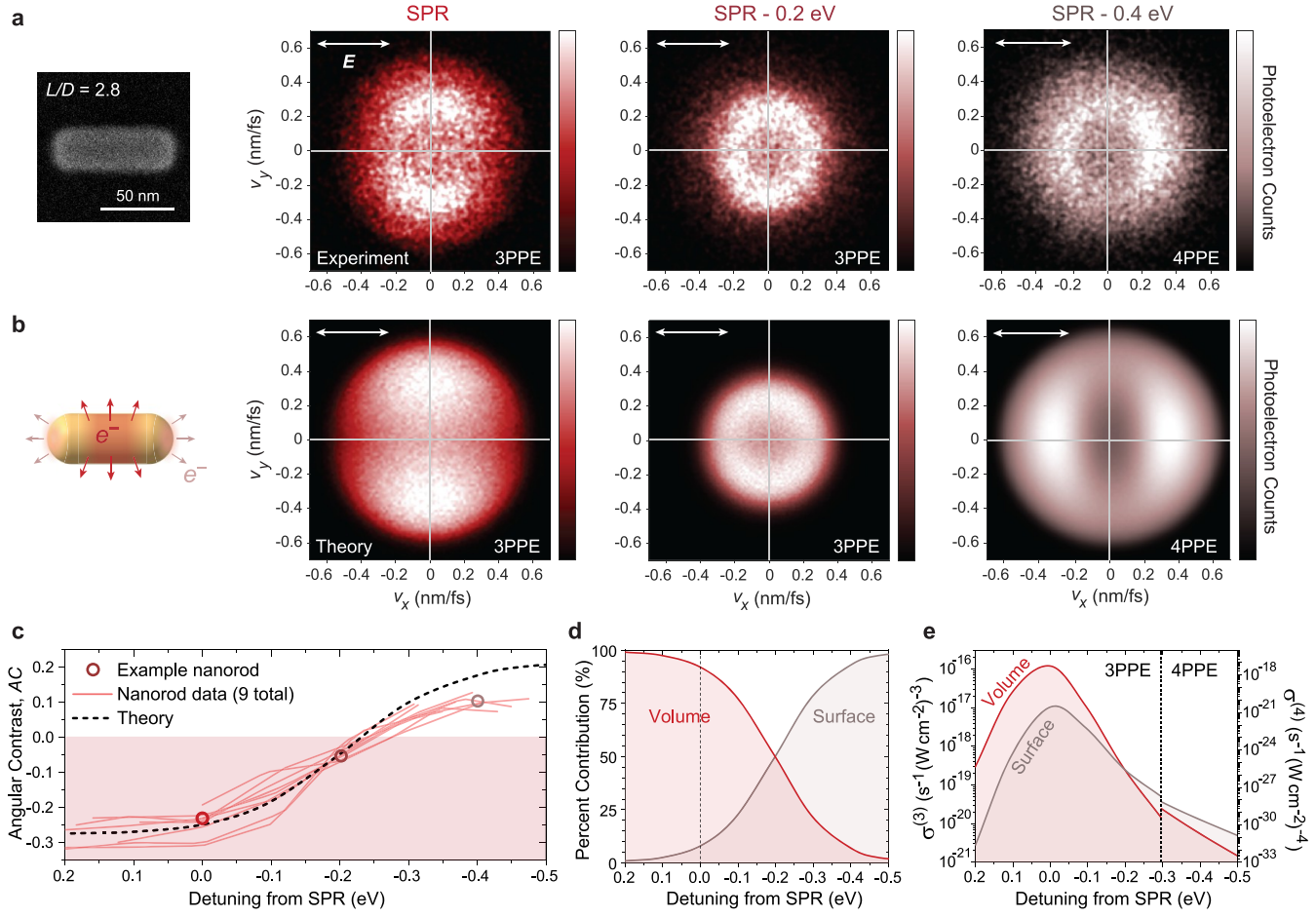

Figure 4. Transition from volume to surface photoemission with red detuning. (a) Experimental and (b) theoretical velocity maps at various detunings from the SPR of the correlated example nanorod, showing the transition from volume (transverse) to surface (longitudinal) photoemission. (c) Summary of angular photoemission contrast values for nine nanorods, with data points for the example rod in (a) and the theoretical curve from (b). All nanorods display consistent behavior and transition from the volume regime (shaded, AC < 0) into the surface regime (AC > 0) around −0.25 eV detuning. (d) Relative volume and surface contributions determined from the fit of $a^{(n)}$ in (c). (e) Volume and surface *n*PPE cross sections for the example nanorod in (a).

hemispherical surface charge distribution at the tips. The corresponding electric field vectors destructively cancel within the tip regions but add constructively near the nanorod center. Such central concentration of the field distributions leads to more centralized excitation of electrons, which subsequently escape almost exclusively from the sides of the nanorods rather than the tips, due to the limiting inelastic mean-free path (∼5 nm). This results in more negative (transverse) angular contrast values compared with uniform excitation throughout the nanorod body, as seen by comparing the two theoretical curves Figure 2e. It should once again be emphasized that this is an entirely different phenomenon from centralized heating effects that have been observed due to higher electron kinetic energies in the center of the nanorod during plasmon oscillations.[7] Thermal effects are negligible in the intensity range ($I_0 \approx 0.05–0.1$ GW cm^{-2}) of these perturbative studies (SI Section 4).

While the overall field enhancement is strongest on the plasmon resonance, the relative surface field contribution increases with red detuning due to enhanced Drude screening of the internal fields at lower frequencies. The ratio of these nonlinear surface *vs* volume field enhancement integrals, which is proportional to the ratio of the surface *vs* volume photoemission, is summarized for different aspect ratios in Figure 3b. The total *n*-photon photoemission rate can be written as

$$n\text{PPE} = (\sigma_S^{(n)}(\omega) + \sigma_V^{(n)}(\omega))I_0^n \tag{2}$$

The generality of eq 2 with respect to coherent *vs* incoherent processes and possible surface−volume cross terms are examined in SI Section 2, with cross terms effectively ruled out due to the large spatial separation between volume and surface-normal field-enhanced regions. Furthermore, previous studies have predominantly found plasmonic *n*PPE to proceed coherently,[4,40,59−61] which is vital to femtosecond (especially <10 fs) electron sources and coherent control applications.[62] Nevertheless, the essential design principles to be discussed would remain valid in the presence of incoherent surface-volume cross terms (SI Section 2). The surface and volume *n*PPE cross sections in eq 2 are given by

$$\sigma_S^{(n)}(\omega) = c_S^{(n)}(\omega)\eta_S^{(n)}(\omega)\int |E_\perp(\mathbf{r},\omega)/E_0|^{2n}\,dS \tag{3a}$$

and

$$\sigma_V^{(n)}(\omega) = c_V^{(n)}(\omega)\eta_V^{(n)}(\omega)\int |E(\mathbf{r},\omega)/E_0|^{2n}\,dV \tag{3b}$$

https://dx.doi.org/10.1021/acsnano.0c09045
ACS Nano 2021, 15, 1566−1578

respectively, in which the $c_S^{(n)}$ and $c_V^{(n)}$ factors are related to the surface and volume nonlinear absorption densities and $\eta_S^{(n)}$ and $\eta_V^{(n)}$ are the emission quantum yields for n-photon excitation. Strictly speaking, the volume emission quantum yield in eq 3b is a volume-averaged quantity:

$$\eta_V^{(n)}(\omega) = \frac{\int \eta_V^{(n)}(\mathbf{r}, \omega)|E(\mathbf{r}, \omega)|^{2n} dV}{\int |E(\mathbf{r}, \omega)|^{2n} dV} \tag{4}$$

which thus depends on the geometry and can be determined *via* ballistic Monte Carlo modeling using the simulated plasmonic fields. Typical values for $\eta_V^{(n)}$ for nanorods are between 0.1% and 1%, as quantified *via* full nanorod surface maps in Figure S8, although this depends strongly on the excitation frequency[63] and may also be substantially enhanced by surface roughness[64] as well as for lower-order processes with smaller barriers such as one-photon photocatalysis and photovoltaics. By comparison, $\eta_s^{(n)}$ only depends on the (generic) properties of the locally flat surface potential barrier and is therefore not geometry specific. As a result, the only geometry-specific quantities are the field enhancement integrals in eqs 3a and 3b, which encode the plasmonic response of the system and can be determined *via* finite element modeling, and $\eta_V^{(n)}$, which can be determined *via* Monte Carlo modeling. The remaining quantities, $c_S^{(n)}\eta_S^{(n)}$ and $c_V^{(n)}$, are properties only of the nanoparticle material and/or nanoparticle−vacuum interface. Thus, if these material quantities are characterized experimentally, then $\sigma_S^{(n)}$ and $\sigma_V^{(n)}$ are fully determined, and the surface *vs* volume contributions may be quantitatively extended to arbitrary nanoscale or even macroscopic geometries.

The 2D angle-resolved photoelectron velocity maps can be utilized to distinguish the volume and surface distributions and separately determine $\sigma_S^{(n)}(\omega)$ and $\sigma_V^{(n)}(\omega)$. Considering the dramatic change in the relative nonlinear surface *vs* volume field enhancements with detuning (Figure 3b), the photoemission is expected to transition from the transverse volume-dominated distribution (AC < 0) that is always observed around the SPR to a longitudinal surface-dominated distribution (AC > 0), with only modest red detuning. This is precisely what is observed in Figure 4a, with the angular contrast summarized in Figure 4c becoming positive around $\Delta\hbar\omega \approx -0.25$ eV detuning. Unlike transverse volume emission, the longitudinal surface emission is often asymmetric due to amplification of any tip field asymmetry (*i.e.*, due to slight tip curvature differences) by the nonlinear process. For example, a 10% difference in the tip fields results in a factor of 2 difference in 4PPE rates ($\propto |E/E_0|^8$). To take such asymmetry into account, the angular contrast values are obtained by averaging over both longitudinal directions (eq 1). The measured angular contrast values for nine sample nanorods resonant between 700−800 nm (L/D = 2.5−3.5) are summarized in Figure 4c, which all display very similar behaviors with detuning. Notably, the range of detuning values crossing AC = 0 is about a factor of 3 narrower than the spread in the SPR energies due to sample heterogeneity, as explicitly shown in Figure S9. This indicates that detuning is the predominant cause of the transition from volume- to surface-dominated photoemission for a specific geometry, with no sudden change observed for the 3PPE−4PPE process order transition at a specific excitation energy. Although higher input intensities are utilized at −0.4 eV red detuning ($I_0 \approx 2$ GW cm^{-2}, compared with ∼0.05 GW cm^{-2} on resonance), this maintains the local tip surface fields by compensating for the drop in the plasmonic enhancement with detuning from resonance, along with a small overcompensation to achieve surface nPPE levels comparable to the volume nPPE levels on resonance. Intensity-dependent measurements (Figure S10) verify that the surface emission at −0.4 eV red detuning remains in the multiphoton regime, rather than the strong-field or thermionic regimes.

For a careful separation of surface and volume contributions, the 3D photoemission distributions (and 2D projections) are modeled for both mechanisms taking the correlated nanorod geometry into account (Figure 4b). Volume photoemission distributions are again calculated *via* the ballistic Monte Carlo method, while the surface nPPE theory developed by Yalunin and co-workers[65] is implemented to model the surface photoemission distributions. The implementation of this surface nPPE theory to arbitrary nanoparticle systems is described in detail in the SI Section 7 and in previous work.[8] The combination of the semiclassical volume Monte Carlo and quantum surface nPPE theories provides a general theoretical framework for modeling 3D photoelectron spatial and momentum distributions in arbitrary nanoplasmonic geometries. In all experiments and theory, the 3D photoelectron velocity distributions are projected/integrated over the v_z degree of freedom, leading to the 2D (v_x,v_y) velocity maps (Methods). Possible effects of the ITO substrate on the 3D distributions and 2D projections are discussed in the SI Sections 6 and 7 and in previous work.[8]

The ratio of the calculated surface *vs* volume contributions, $\sigma_S^{(n)}/\sigma_V^{(n)}$, depends on the ratio of the field integrals (Figure 3b) as well as the geometry-independent coefficients in eqs 3a and 3b. In the near-threshold photoemission regime with excess photoelectron kinetic energies < 2 eV, the frequency dependence of both surface and volume coefficients is expected to obey Fowler's law,[63] such that $c_S^{(n)}(\omega)\eta_S^{(n)}(\omega) \propto c_V^{(n)}(\omega)\eta_V^{(n)}(\omega) \propto (n\hbar\omega - \phi)^2$, which thus cancels out in the $\sigma_S^{(n)}/\sigma_V^{(n)}$ ratio. As a result, all of the frequency dependence in $\sigma_S^{(n)}/\sigma_V^{(n)}$ is contained within the ratio of the nonlinear field integrals, scaled by a single frequency-independent prefactor:

$$a^{(n)} = \frac{c_S^{(n)}(\omega)\eta_S^{(n)}(\omega)}{c_V^{(n)}(\omega)\eta_V^{(n)}(\omega)} \tag{5}$$

Thus, the role of experiment in determining the relative photoemission contributions is reduced to determining this single, frequency-independent $a^{(n)}$ parameter for different process orders.

Weighting the modeled surface and volume photoemission distributions by the field integral ratio from Figure 3b, we find that $a^{(3)} = 7.5 \pm 2.5$ pm yields the best agreement with the experimental angular contrast as a function of detuning (Figure 4c). The relative surface and volume contributions are now quantified, as shown in Figure 4d, with volume mechanisms accounting for 90% of the total photoemission on resonance. The corresponding 10% surface contribution on resonance accounts for the slightly less negative (less transverse) experimental angular contrast values in Figure 2e relative to the purely volume Monte Carlo theory. Finally, with $\sigma_S^{(n)}/\sigma_V^{(n)}$ now determined and $\sigma_S^{(n)} + \sigma_V^{(n)}$ known directly from the total experimentally measured photoemission rates (eq 2), $\sigma_S^{(n)}$ and $\sigma_V^{(n)}$ can be determined independently, as summarized in Figure 4e for the representative nanorod. We note that $\sigma_S^{(n)}$ and $\sigma_V^{(n)}$ are only directly determined in the 3PPE range. While $a^{(n)}$

https://dx.doi.org/10.1021/acsnano.0c09045
ACS Nano 2021, 15, 1566−1578

could be directly determined for other process orders *via* additional detuning studies, we instead simply rely on the approximate continuity in experimental $\sigma_S^{(n)}/\sigma_V^{(n)}$ curves (*i.e.*, no sudden changes observed with detuning) from the $L/D \approx 3$ nanorod detuning studies in Figure 4 to extend the 3-photon results into the adjacent 2- and 4-photon ranges. With the aid of finite element and Monte Carlo modeling of the geometry-specific quantities (field integrals and escape efficiencies, respectively), this in principle now allows us to quantitatively predict the photoemission behaviors for arbitrary gold nanoparticle geometries.

General Design Principles. It has been shown that the plasmonic field enhancements are of primary importance in determining the relative surface and volume contributions to electron emission. With $a^{(3)}$ (eq 5) and the nanomaterial-specific properties in eqs 3a and 3b determined from detuning experiments, the effects of optical parameters and nanoparticle geometry can now be quantitatively estimated, including the effects of (i) frequency-dependent electric field screening, (ii) geometric surface-to-volume (S/V) ratio, and (iii) nanoparticle shape/curvature. We shall demonstrate that optical parameters influence the relative surface *vs* volume contributions primarily *via* frequency-dependent screening, while the nanoparticle shape controls the plasmonic field distribution at constant excitation frequency. As noted in the previous section, results from the 3PPE range (Figure 4) are approximately extended into the 2PPE and 4PPE ranges based on the observed continuity in $\sigma_S^{(n)}/\sigma_V^{(n)}$.

First, we consider the effects of frequency-dependent screening and the plasmon resonance (Figure 5a) on the surface *vs* volume photoemission contributions. Specifically, plasmonic field enhancements and resulting $\sigma_S^{(n)}/\sigma_V^{(n)}$ ratios are simulated for ligand-free nanorods in vacuum, for a series of aspect ratios (Figure 5a). With this environment, the surface field enhancements are more prominent, and longer nanorods are predicted to be surface emitters on resonance, unlike the ligand-coated, ITO-supported nanorods studied experimentally. For nanospheres in the electrostatic approximation and $\mathbf{E}_0 = E_0\hat{x}$, the Laplace equation yields a constant internal field:[66]

$$E_{in}(\omega) = \frac{3\epsilon_0}{\epsilon(\omega) + 2\epsilon_0} E_0\hat{x} \tag{6a}$$

and a dipolar external field at the nanosphere surface:

$$E_{out}(\omega) = E_0\hat{x} + \frac{\epsilon(\omega) - \epsilon_0}{\epsilon(\omega) + 2\epsilon_0}(3E_0\hat{n} - E_0\hat{x}) \tag{6b}$$

where $\epsilon(\omega)$ is the dielectric function of the nanosphere material (*e.g.*, gold) and $\hat{n}$ is the outward surface normal. The external field at the nanosphere "tip" along the laser polarization axis ($\hat{n} = \hat{x}$) is

$$E_{tip}(\omega) = \frac{3\epsilon(\omega)}{\epsilon(\omega) + 2\epsilon_0} E_0\hat{x} \tag{7}$$

from which the resulting ratio of the external-to-internal electric field at the tip is given simply by

$$\frac{E_{tip}(\omega)}{E_{in}(\omega)} = \frac{\epsilon(\omega)}{\epsilon_0} \tag{8}$$

This can also be immediately derived from the boundary condition on the displacement field, $\mathbf{D}_{in}\cdot\hat{n} = \mathbf{D}_{out}\cdot\hat{n}$, yielding

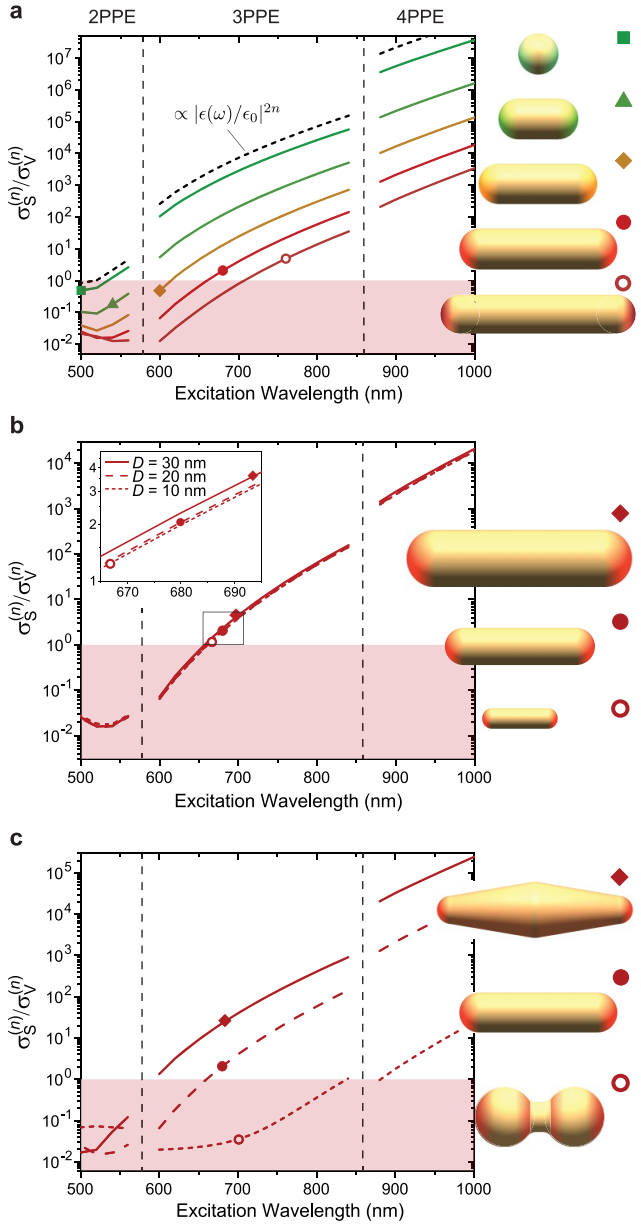

Figure 5. Effects of screening, S/V ratio, and nanoparticle geometry (curvature) on surface and volume contributions. This set of simulations is performed in vacuum (no ligands or substrate). Shading indicates the volume-dominated regime. (a) Surface/volume *n*PPE cross-section ratio determined quantitatively from detuning studies (Figure 4) for L/D = 1−5 nanorods. Points indicate plasmon resonance wavelength. The dashed curve is the dielectric function of gold (arbitrary scale factor), which evidently dictates the frequency dependence of the surface/volume cross-section ratios. (b) Cross-section ratio for L/D = 4 nanorod for D = 10−30 nm, with zoomed-in inset. (c) Cross-section ratio for bipyramid, nanorod, and dumbbell, all with similar resonance, S/V ratio (< 10% variation), and total V (< 30% variation).

$\epsilon(\omega)E_{in}(\omega) = \epsilon_0 E_{tip}(\omega)$. The crucial result is that the plasmonic resonance term, $\propto (\epsilon(\omega) + 2\epsilon_0)^{-1}$, drops out of the field ratio in eq 8 entirely, and we are left only with the screening effects described by the metal dielectric function, $\epsilon(\omega)$. Furthermore, the same cancellation of the surface and volume plasmonic field enhancements occurs in the full nonlinear field integrals, leading to $\sigma_S^{(n)}/\sigma_V^{(n)} \propto |\epsilon(\omega)/\epsilon_0|^{2n}$, as shown in Figure 5a. Thus, the dramatic increase in surface over volume photoemission at

https://dx.doi.org/10.1021/acsnano.0c09045
ACS Nano 2021, 15, 1566−1578

longer wavelengths can be simply attributed to enhanced metallic screening of internal fields. At a constant excitation wavelength, the progressive overall drop in $\sigma_S^{(n)}/\sigma_V^{(n)}$ with increasing nanorod aspect ratio in Figure 5a is due to details of the nanorod geometry and plasmonic field distributions.

Next, we consider the effects of nanoparticle scale (Figure 5b). The importance of the geometric S/V ratio has been emphasized in other investigations,[14] but it has remained unclear whether this is truly the decisive factor, in general, due to the previous lack of direct mechanistic insight into the excitation processes. Here, we isolate the effect of S/V ratio by investigating nanorods with the same aspect ratio but different diameters (Figure 5b). By maintaining the same nanorod shape, the field enhancement distributions and SPRs remain approximately constant with size, with a 3-fold change in the S/V ratio from 0.44 nm^{-1} (D = 10 nm) to 0.15 nm^{-1} (D = 30 nm). This factor of 3 is relatively minor compared with the orders-of-magnitude changes in $\sigma_S^{(n)}/\sigma_V^{(n)}$ with only modest frequency detuning. Moreover, a commensurate change in the volume emission efficiency with nanoparticle size, $1/\eta_V^{(n)} \propto D$, effectively cancels the $S/V \propto D^{-1}$ contribution to $\sigma_S^{(n)}/\sigma_V^{(n)}$. This occurs for larger particles ($D \gg \lambda_{inel}$) in which the ratio of electrons excited within the escape depth from the surface ($\sim \lambda_{inel}$) to the total number of electrons excited throughout the nanoparticle approaches the geometric S/V ratio,[13] such that the escape efficiency scales as S/V ($\eta_V^{(n)} \propto D^{-1}$). Thus, $\sigma_S^{(n)}/\sigma_V^{(n)}$ remains nearly constant with nanoparticle scale at fixed excitation frequency, as shown in Figure 5b. It is not until particle dimensions become comparable to or smaller than the electron inelastic mean-free path that the $S/V \propto D^{-1}$ scaling begins to take over.[13] This $\sigma_S^{(n)}/\sigma_V^{(n)} \propto D^{-1}$ regime may nonetheless be relevant for low-energy catalysis (*e.g.*, $\lambda_{inel} \approx 40$ nm for gold at ~1.5 eV excitation energy) with small nanoparticles (D < 30 nm).

Finally, we consider the effects of nanoparticle shape (Figure 5c). While the effect of nanoparticle size/scale is generally minor, the nanoparticle shape strongly influences $\sigma_S^{(n)}/\sigma_V^{(n)}$ *via* the plasmonic field distributions. It is well known that sharp convex features, for instance, lead to more dramatic surface field enhancements due to the lightning rod effect,[62,67] whereas flat or concave features can shift emphasis to the volume fields. The role of nanoparticle curvature is effectively isolated by comparing particles of different shapes but similar SPR, S/V ratio, and total volume (see Figure 5c). Sharper geometries, such as bipyramids, exhibit more concentrated surface field enhancements and more diffuse volume enhancements (Figure S13), leading to an enhanced surface photoemission contribution. This is corroborated by *n*PPE microscopy observations of tip-localized photoemission from silver bipyramids[68] and gold nanostars,[8,69] along with *n*PPE studies of etched gold nanotips.[62] Conversely, geometries with lower curvature and/or concave features, such as dumbbells in Figure 5c, display much weaker surface fields and stronger relative interior field enhancements (Figure S13), leading to dominant volume photoemission. As it happens, nanorods strike a delicate balance between these extremes, which makes them excellent testbeds for distinguishing general surface *vs* volume photoemission properties.

Interestingly, the effect of shape on internal quantum efficiency, $\eta_V^{(n)}$, is typically very minor. For example, $\eta_V^{(3)}$ = 0.27% for the L/D = 4 resonantly excited nanorod in Figure 5c, while $\eta_V^{(3)}$ = 0.32% for the dumbbell excited at nearly the same SPR frequency. We also note that these rather small internal quantum efficiencies are due in part to the small fraction of photoexcited electrons above the vacuum level for the multiphoton excitation ($\lesssim$ 20%) along with escape cone effects,[50] both of which are dramatically improved in single-photon photovoltaic and photocatalytic collection schemes with much larger fractions of excited carriers at/above the relevant energy barriers. Considering the small variation of $\eta_V^{(n)}$ with nanoparticle shape, the strong influence the shape has on $\sigma_S^{(n)}/\sigma_V^{(n)}$ demonstrated in Figure 5c therefore arises primarily from the shape-dependent distribution and concentration of plasmonic fields, rather than the volume escape efficiency. This has two significant benefits for designing plasmonic devices: (i) the plasmonic fields can be readily simulated by a variety of classical methods (*e.g.*, finite element simulation), and (ii) a further degree of optical control—beyond frequency-dependent screening—can be readily exerted by coupling to different plasmon resonance modes *via* laser polarization and/or frequency. Different plasmon resonance modes will display different volume and surface field distributions, with the latter already having been utilized, for instance, to control photocurrents from gold nanostars with multiple tip hot spots.[8,69]

Conversely, we note as a parting comment that photoemission angular distributions may be utilized to elucidate nanoplasmonic field distributions for different optical parameters and particle geometries, providing complementary information to photoemission spatial distributions from photoemission electron microscopy (PEEM) studies.[9,68,69] While PEEM spatial maps with tens-of-nanometer resolution provide a clear indication of hot spots and emissive regions correlated with nanoscale structure, single-nanoparticle angle-resolved photoemission studies[5,8,49,70] can provide further details on the (3D) field distributions, so long as the photoexcitation/emission dynamics can be accurately modeled. Thus, with insights from the present studies, these and other *n*PPE techniques may be utilized to complement electron energy loss spectroscopy,[71] super-resolution imaging,[72] and scanning near-field optical techniques[7374,75] for mapping nanophotonic fields.

CONCLUSIONS

In summary, we have demonstrated the essential roles of nanoscopic volume *vs* surface photoexcitation mechanisms in nanoplasmonic electron emission, along with corresponding opportunities for designing and optically controlling excited electron spatial and momentum distributions. Volume excitation is found to be dominant for nanorods excited on resonance, producing energetic electrons near the center of the nanorods that subsequently escape from the nearby side surfaces in transverse photoemission distributions relative to the nanorod axis. However, red detuning of the excitation laser from resonance strongly de-emphasizes the volume fields due to enhanced metallic screening, instead promoting photoexcitation directly at the tip surfaces. The surface-excited electrons are preferentially emitted longitudinally along the nanorod axis and therefore exhibit completely different spatial and momentum distributions compared with the volume-excited electrons. Both mechanisms must be considered in general nanoplasmonic applications, as the relative contributions depend sensitively on nanoparticle shape and frequency-dependent screening. A comprehensive volume (ballistic Monte Carlo) and surface (fully quantum) *n*PPE theoretical framework has been introduced to model these behaviors, illustrating that the plasmonic field enhancement distributions

https://dx.doi.org/10.1021/acsnano.0c09045
ACS Nano 2021, 15, 1566−1578

are critical in controlling surface *vs* volume excitation, while geometric ratios (S/V) and the escape quantum efficiencies ($\eta_V^{(n)}$) play only minor roles. Therefore, upon characterizing the material-specific quantities in the (nonlinear) photoexcitation, as we have done here for gold, the surface *vs* volume photoemission properties of arbitrary nanoplasmonic geometries can be predicted simply *via* classical electromagnetic simulations. These results set the stage for designer geometric and ultrafast optical (polarization and frequency) control over nanocathode photoemission, photovoltaic currents, and site-selective nanocatalytic charge transfer.

METHODS

Nanorod Synthesis and Sample Preparation. Gold nanospheres and nanorods of various sizes and aspect ratios have been synthesized using well-known seed-mediated methods.[76−78] Small gold precursor particles are prepared in the desired solvent (water, in this case) and exposed to additional gold salt in the presence of a reducing agent that promotes controlled growth onto the precursor particles. For nanospheres, the seed concentration in the growth solution is controlled for size uniformity, where more seeds result in smaller nanospheres. The gold nanorods are controlled in their size and aspect ratio by controlling both the seed concentration and the concentration of silver nitrate—a growth-directing agent—in the solution. The details of each synthesis procedure and the reagents used are described in detail in the SI Section 3.

Following synthesis, the nanosphere and nanorod solutions are sonicated for 30 s and vortexed for 10 s for optimal dispersion, then diluted in ultrapure water to approximately 0.1 nM (6×10^{10} nanoparticles mL^{-1}). Immediately following dilution, a 50 μL aliquot is spin-coated onto a freshly UV-ozone cleaned ITO-coated coverslip (10 nm ITO sputtered on 170 μm borosilicate; Thin Film Devices, Inc.) at 1500 rpm for 5 min. For aqueous nanoparticle solutions, this procedure yields a typical coverage of 0.05 nanoparticles μm^{-2}, or 20 particles in a 20×20 μm^2 scan area on average. Such coverages are ideal for efficient particle location and characterization *via* SPIM scans, while ensuring negligible probability of two particles overlapping within the same diffraction-limited excitation region. For particle location in correlated SPIM-SEM studies, a 30 nm Au alphanumeric grid (LF-400) is deposited onto all ITO/glass substrates *via* negative photomask lithography, prior to sample preparation.

Scanning Photoelectron Imaging Microscopy. Photoemission microscopy using a home-built scanning sample stage allows for spatially resolved (diffraction-limited) photoemission mapping.[4] Three quartered piezoelectric posts with capacitive sensor feedback provide fine scanning over a 30×30 μm^2 area, with *xyz* piezo motors providing extended positioning over a larger (few-millimeter) range. Single particles are identified and studied individually, with the total photoemission rate measured as a function of laser frequency, intensity, and polarization. Combined with correlated SEM imaging and finite element simulation, this already provides detailed near-field information on the photoemission properties of the plasmonic nanoparticles. To get additional information on excited electron spatial and angular distributions, essential for the present studies, we employ a three-electrode velocity map imaging (VMI) electrostatic lens for photoelectron velocity mapping. The VMI lens provides a linear mapping from initial (v_x, v_y) velocities onto (x, y) spatially resolved microchannel plate detector (two-plate chevron configuration) position, simply integrating the initial 3D distribution over v_z. A single electron is multiplied up to $\sim 10^7$ electrons, and the amplified electron signal is then accelerated onto a P47 phosphor screen, with the fluorescence imaged *via* CCD camera (1.3 megapixels, 20 FPS). Single event (x, y) coordinates are centroided and converted back to (v_x, v_y) velocity *via* a calibration factor of 4150 m s^{-1} px^{-1} measured previously.[49] Further details on the SPIM system and velocity mapping can be found in previous work.[49]

Femtosecond pulses are generated a 75 MHz Ti:sapphire oscillator (KMLabs Swift, 675−1000 nm), with second-harmonic generation (350−500 nm) and an optical parametric oscillator (KMLabs, 510−780 nm signal tuning range) providing broad tunability from the UV to the near-IR. A high-vacuum compatible ($< 5 \times 10^{-7}$ Torr) reflective Cassegrain microscope objective (NA = 0.65) focuses the pulsed laser beams to a diffraction-limited spot (~500 nm spot diameter) on the sample at normal incidence, as shown in Figure 1a. For optimal frequency tunability without spatial walk-off, no external prism dispersion compensation is utilized for the majority of the present studies. Group velocity dispersion in the system thus results in 100−200 fs pulse durations at the sample across the laser tuning range. As a check, several measurements have also been performed with dispersion-compensated 40−50 fs pulses and found to yield indistinguishable nanorod photoemission velocity distributions. Nanorods are cleaned prior to all studies *via* brief (~1 s) exposure to ~1 GW cm^{-2} of second-harmonic light (400 nm), which removes adlayers (e.g., water) that develop during brief sample exposure to ambient air.[79]

Scanning Electron Microscopy (SEM). Correlated SEM (FEI Nova NanoSEM 630, 10 kV, $< 1 \times 10^{-5}$ Torr, through-lens detector, field immersion mode) is performed on every gold nanorod and nanosphere investigated. The conductive ITO film on the glass substrate provides a route for charge dissipation during imaging. While no particle morphology changes are observed during imaging, micrographs are always collected following SPIM studies to avoid particle degradation due to electron beam exposure and concomitant amorphous carbon buildup. The Au reference grid is utilized to locate the nanoparticles in both SPIM and SEM, whereby the relative particle orientation is determined to within a few degrees by the grid orientation and the particle distribution within a grid area.

Finite Element Method. Finite element simulations of the plasmonic electric field enhancements are performed using the RF module in COMSOL Multiphysics 5.4. For supported nanorod and nanosphere simulations, a 1.5 nm cetyltrimethylammonium bromide (CTAB) ligand layer surrounding the particles is included in the simulations, along with an additional 0.5 nm gap between the ligand layer and the substrate to avoid extra-narrow domain regions. Overall, the rectangular domain consists of the glass substrate with a 10 nm ITO film, the vacuum superstrate, the gold nanoparticle with ligand layer, and a perfectly matched layer surrounding the domain to prevent field reflection at the domain boundaries. The numerical solution to Maxwell's equations includes the dipolar and higher-order charge oscillation modes, although only dipolar modes are found to contribute substantially in the present frequency and nanorod size range. The effect of the transparent conducting substrate image charge oscillation is to enhance the field on the lower half of the nanorod, as accounted for in the Monte Carlo and surface *n*PPE modeling and discussed in the SI Sections 6 and 7, respectively. Nanorods are modeled as perfect cylinders with hemispherical end-caps, with diameter D and total tip-to-tip length L. Triangular surface and tetrahedral volume meshing were constructed with near-uniform element size across the nanoparticle surface/volume, with the element side length (2 nm) selected to be much smaller than the nanoparticle dimensions and any electric field variation on the surface or within the volume. This is particularly essential, as the same mesh and calculated field values at the vertices are subsequently utilized for both volume and surface photoemission modeling. The optical constants of gold are taken from the literature[80] and determined for the ITO film *via* ellipsometry. We utilized $n_{lig} = 1.5$ and $k_{lig} = 0.25$ for the CTAB ligand layer, where the small extinction coefficient accounts for the presence of amorphous carbon due to the hot-electron-driven conversion of the organic ligands. Further discussion of this conversion process and nanorod photoemission stability can be found in the SI Section 9.

Code and Materials Availability. All data required to reproduce the results presented here are available within the paper, the Supporting Information, or from the corresponding authors upon reasonable request. All code is available from D.J.N. upon reasonable request.

https://dx.doi.org/10.1021/acsnano.0c09045
ACS Nano 2021, 15, 1566−1578

ASSOCIATED CONTENT

Supporting Information

The Supporting Information is available free of charge at https://pubs.acs.org/doi/10.1021/acsnano.0c09045.

Volume *vs* surface photoexcitation, coherent *vs* incoherent photoexcitation, nanorod synthesis and characterization, multiphoton *vs* thermionic or optical field emission, effects of nanorod diameter and surface ligands, volume photoemission modeling, surface photoemission modeling, red detuning effects, nanorod stability, and surface and volume field distributions (PDF)

AUTHOR INFORMATION

Corresponding Authors

David J. Nesbitt − *JILA, University of Colorado Boulder and National Institute of Standards and Technology, Boulder, Colorado 80309, United States; Department of Physics and Department of Chemistry, University of Colorado Boulder, Boulder, Colorado 80309, United States;* orcid.org/0000-0001-5365-1120; Email: djn@jila.colorado.edu

Catherine J. Murphy − *Department of Chemistry and Materials Research Laboratory, University of Illinois at Urbana−Champaign, Urbana, Illinois 61801, United States;* orcid.org/0000-0001-7066-5575; Email: murphycj@illinois.edu

Authors

Jacob Pettine − *JILA, University of Colorado Boulder and National Institute of Standards and Technology, Boulder, Colorado 80309, United States; Department of Physics, University of Colorado Boulder, Boulder, Colorado 80309, United States;* orcid.org/0000-0003-2102-1743

Sean M. Meyer − *Department of Chemistry, University of Illinois at Urbana−Champaign, Urbana, Illinois 61801, United States;* orcid.org/0000-0003-0771-5095

Fabio Medeghini − *JILA, University of Colorado Boulder and National Institute of Standards and Technology, Boulder, Colorado 80309, United States;* orcid.org/0000-0002-0508-3365

Complete contact information is available at: https://pubs.acs.org/10.1021/acsnano.0c09045

Author Contributions

J.P., F.M., and D.J.N designed the experiments. J.P. executed the experiments, performed the analysis, and developed the theoretical methods with help from F.M., under the supervision of D.J.N. S.M.M. synthesized and characterized the nanorods and nanospheres under the supervision of C.J.M. The manuscript was written with contributions and final approval from all authors.

Notes

The authors declare no competing financial interest.

ACKNOWLEDGMENTS

This work has been supported by the Air Force Office of Scientific Research (FA9550-15-1-0090) with additional funds for laser and apparatus development provided by the National Science Foundation Physics Frontier Center (PHY-1734006). Support for nanoparticle synthesis and characterization in the C.J.M. laboratory has been funded by the National Science Foundation (CHE-1608743). The authors would like to thank Dr. J. G. Hinman for contributions to the synthetic procedures and Prof. H. Petek for discussions regarding this work.

REFERENCES

(1) Bonzel, H. P.; Kleint, C. On the History of Photoemission. *Prog. Surf. Sci.* **1995**, *49* (2), 107−153.

(2) Aeschlimann, M.; Bauer, M.; Bayer, D.; Brixner, T.; Cunovic, S.; Dimler, F.; Fischer, A.; Pfeiffer, W.; Rohmer, M.; Schneider, C.; Steeb, F.; Strüber, C.; Voronine, D. V. Spatiotemporal Control of Nanooptical Excitations. *Proc. Natl. Acad. Sci. U. S. A.* **2010**, *107* (12), 5329−5333.

(3) Dombi, P.; Hörl, A.; Rácz, P.; Márton, I.; Trügler, A.; Krenn, J. R.; Hohenester, U. Ultrafast Strong-Field Photoemission from Plasmonic Nanoparticles. *Nano Lett.* **2013**, *13* (2), 674−678.

(4) Grubisic, A.; Schweikhard, V.; Baker, T. A.; Nesbitt, D. J. Coherent Multiphoton Photoelectron Emission from Single Au Nanorods: The Critical Role of Plasmonic Electric Near-Field Enhancement. *ACS Nano* **2013**, *7* (1), 87−99.

(5) Lehr, M.; Foerster, B.; Schmitt, M.; Krüger, K.; Sönnichsen, C.; Schönhense, G.; Elmers, H. J. Momentum Distribution of Electrons Emitted from Resonantly Excited Individual Gold Nanorods. *Nano Lett.* **2017**, *17* (11), 6606−6612.

(6) Cortes, E.; Xie, W.; Cambiasso, J.; Jermyn, A. S.; Sundararaman, R.; Narang, P.; Schlucker, S.; Maier, S. A. Plasmonic Hot Electron Transport Drives Nano-Localized Chemistry. *Nat. Commun.* **2017**, *8*, 14880.

(7) Hobbs, R. G.; Putnam, W. P.; Fallahi, A.; Yang, Y.; Kärtner, F. X.; Berggren, K. K. Mapping Photoemission and Hot-Electron Emission from Plasmonic Nanoantennas. *Nano Lett.* **2017**, *17* (10), 6069−6076.

(8) Pettine, J.; Choo, P.; Medeghini, F.; Odom, T. W.; Nesbitt, D. J. Plasmonic Nanostar Photocathodes for Optically-Controlled Directional Currents. *Nat. Commun.* **2020**, *11*, 1367.

(9) Dąbrowski, M.; Dai, Y.; Petek, H. Ultrafast Photoemission Electron Microscopy: Imaging Plasmons in Space and Time. *Chem. Rev.* **2020**, *120* (13), 6247−6287.

(10) Tamm, I.; Schubin, S. On the Theory of the Photoelectric Effect in Metals. *Eur. Phys. J. A* **1931**, *68* (1−2), 97−113.

(11) Glasser, M. L.; Bagchi, A. Theories of Photoemission from Metal Surfaces. *Prog. Surf. Sci.* **1976**, *7* (3), 113−148.

(12) Miller, T.; McMahon, W. E.; Chiang, T. C. Interference between Bulk and Surface Photoemission Transitions in Ag(111). *Phys. Rev. Lett.* **1996**, *77* (6), 1167−1170.

(13) Uskov, A. V.; Protsenko, I. E.; Ikhsanov, R. S.; Babicheva, V. E.; Zhukovsky, S. V.; Lavrinenko, A. V.; O'Reilly, E. P.; Xu, H. X. Internal Photoemission from Plasmonic Nanoparticles: Comparison between Surface and Volume Photoelectric Effects. *Nanoscale* **2014**, *6* (9), 4716−4727.

(14) Graf, M.; Jalas, D.; Weissmuller, J.; Petrov, A. Y.; Eich, M. Surface-to-Volume Ratio Drives Photoelelectron Injection from Nanoscale Gold into Electrolyte. *ACS Catal.* **2019**, *9* (4), 3366−3374.

(15) Pendry, J. B. Theory of Photoemission. *Surf. Sci.* **1976**, *57* (2), 679−705.

(16) Cortes, E. Efficiency and Bond Selectivity in Plasmon-Induced Photochemistry. *Adv. Opt. Mater.* **2017**, *5* (15), 1700191.

(17) Aslam, U.; Rao, V. G.; Chavez, S.; Linic, S. Catalytic Conversion of Solar to Chemical Energy on Plasmonic Metal Nanostructures. *Nat. Catal.* **2018**, *1* (9), 656−665.

(18) Knight, M. W.; Wang, Y. M.; Urban, A. S.; Sobhani, A.; Zheng, B. Y.; Nordlander, P.; Halas, N. J. Embedding Plasmonic Nanostructure Diodes Enhances Hot Electron Emission. *Nano Lett.* **2013**, *13* (4), 1687−1692.

(19) Karnetzky, C.; Zimmermann, P.; Trummer, C.; Sierra, C. D.; Wörle, M.; Kienberger, R.; Holleitner, A. Towards Femtosecond On-Chip Electronics Based on Plasmonic Hot Electron Nano-Emitters. *Nat. Commun.* **2018**, *9*, 2471.

(20) Mahan, G. D. Theory of Photoemission in Simple Metals. *Phys. Rev. B* **1970**, *2* (11), 4334−4350.

(21) Petek, H. Photoexcitation of Adsorbates on Metal Surfaces: One-Step or Three-Step. *J. Chem. Phys.* **2012**, *137* (9), 091704.
(22) Levinson, H. J.; Plummer, E. W.; Feibelman, P. J. Effects on Photoemission of the Spatially Varying Photon Field at a Metal-Surface. *Phys. Rev. Lett.* **1979**, *43* (13), 952−955.
(23) Khurgin, J. B. Ultimate Limit of Field Confinement by Surface Plasmon Polaritons. *Faraday Discuss.* **2015**, *178*, 109−122.
(24) Broudy, R. M. Vectorial Photoelectric Effect. *Phys. Rev. B* **1971**, *3* (11), 3641.
(25) Pedersoli, E.; Greaves, C. M. R.; Wan, W.; Coleman-Smith, C.; Padmore, H. A.; Pagliara, S.; Cartella, A.; Lamarca, F.; Ferrini, G.; Galimberti, G.; Montagnese, M.; dal Conte, S.; Parmigiani, F. Surface and Bulk Contribution to Cu(111) Quantum Efficiency. *Appl. Phys. Lett.* **2008**, *93* (18), 183505.
(26) Podbiel, D.; Kahl, P.; Makris, A.; Frank, B.; Sindermann, S.; Davis, T. J.; Giessen, H.; Horn-Von Hoegen, M.; Heringdorf, F. J. M. Z. Imaging the Nonlinear Plasmoemission Dynamics of Electrons from Strong Plasmonic Fields. *Nano Lett.* **2017**, *17* (11), 6569−6574.
(27) Babicheva, V. E.; Zhukovsky, S. V.; Ikhsanov, R. S.; Protsenko, I. E.; Smetanin, I. V.; Uskov, A. Hot Electron Photoemission from Plasmonic Nanostructures: The Role of Surface Photoemission and Transition Absorption. *ACS Photonics* **2015**, *2* (8), 1039−1048.
(28) Pettine, J.; Marton Menendez, A.; Nesbitt, D. J. Continuous Angular Control over Anisotropic Photoemission from Isotropic Gold Nanoshells. *J. Chem. Phys.* **2020**, *153* (10), 101101.
(29) Zhang, X.; Li, X. Q.; Zhang, D.; Su, N. Q.; Yang, W. T.; Everitt, H. O.; Liu, J. Product Selectivity in Plasmonic Photocatalysis for Carbon Dioxide Hydrogenation. *Nat. Commun.* **2017**, *8*, 14542.
(30) Mubeen, S.; Lee, J.; Singh, N.; Kramer, S.; Stucky, G. D.; Moskovits, M. An Autonomous Photosynthetic Device in Which All Charge Carriers Derive from Surface Plasmons. *Nat. Nanotechnol.* **2013**, *8* (4), 247−251.
(31) Wu, B. H.; Liu, D. Y.; Mubeen, S.; Chuong, T. T.; Moskovits, M.; Stucky, G. D. Anisotropic Growth of TiO_2 onto Gold Nanorods for Plasmon-Enhanced Hydrogen Production from Water Reduction. *J. Am. Chem. Soc.* **2016**, *138* (4), 1114−1117.
(32) Burrows, N. D.; Lin, W.; Hinman, J. G.; Dennison, J. M.; Vartanian, A. M.; Abadeer, N. S.; Grzincic, E. M.; Jacob, L. M.; Li, J.; Murphy, C. J. Surface Chemistry of Gold Nanorods. *Langmuir* **2016**, *32* (39), 9905−9921.
(33) Sambur, J. B.; Chen, T. Y.; Choudhary, E.; Chen, G. Q.; Nissen, E. J.; Thomas, E. M.; Zou, N. M.; Chen, P. Sub-Particle Reaction and Photocurrent Mapping to Optimize Catalyst-Modified Photoanodes. *Nature* **2016**, *530*, 77−93.
(34) Knight, M. W.; Sobhani, H.; Nordlander, P.; Halas, N. J. Photodetection with Active Optical Antennas. *Science* **2011**, *332* (6030), 702−704.
(35) Brongersma, M. L.; Halas, N. J.; Nordlander, P. Plasmon-Induced Hot Carrier Science and Technology. *Nat. Nanotechnol.* **2015**, *10* (1), 25−34.
(36) Clavero, C. Plasmon-Induced Hot-Electron Generation at Nanoparticle/Metal-Oxide Interfaces for Photovoltaic and Photocatalytic Devices. *Nat. Photonics* **2014**, *8* (2), 95−103.
(37) Wu, K.; Chen, J.; McBride, J. R.; Lian, T. Efficient Hot-Electron Transfer by a Plasmon-Induced Interfacial Charge-Transfer Transition. *Science* **2015**, *349* (6248), 632−635.
(38) Hobbs, R. G.; Yang, Y.; Fallahi, A.; Keathley, P. D.; De Leo, E.; Kärtner, F. X.; Graves, W. S.; Berggren, K. K. High-Yield, Ultrafast, Surface Plasmon-Enhanced, Au Nanorod Optical Field Electron Emitter Arrays. *ACS Nano* **2014**, *8* (11), 11474−11482.
(39) Müller, M.; Paarmann, A.; Ernstorfer, R. Femtosecond Electrons Probing Currents and Atomic Structure in Nanomaterials. *Nat. Commun.* **2014**, *5*, 5292.
(40) Müller, M.; Kravtsov, V.; Paarmann, A.; Raschke, M. B.; Ernstorfer, R. Nanofocused Plasmon-Driven Sub-10 fs Electron Point Source. *ACS Photonics* **2016**, *3* (4), 611−619.
(41) Tan, S. J.; Argondizzo, A.; Ren, J. D.; Liu, L. M.; Zhao, J.; Petek, H. Plasmonic Coupling at a Metal/Semiconductor Interface. *Nat. Photonics* **2017**, *11* (12), 806−812.
(42) Link, S.; El-Sayed, M. A. Spectral Properties and Relaxation Dynamics of Surface Plasmon Electronic Oscillations in Gold and Silver Nanodots and Nanorods. *J. Phys. Chem. B* **1999**, *103* (40), 8410−8426.
(43) Schmucker, A. L.; Harris, N.; Banholzer, M. J.; Blaber, M. G.; Osberg, K. D.; Schatz, G. C.; Mirkin, C. A. Correlating Nanorod Structure with Experimentally Measured and Theoretically Predicted Surface Plasmon Resonance. *ACS Nano* **2010**, *4* (9), 5453−5463.
(44) Putnam, W. P.; Hobbs, R. G.; Keathley, P. D.; Berggren, K. K.; Kärtner, F. X. Optical-Field-Controlled Photoemission from Plasmonic Nanoparticles. *Nat. Phys.* **2017**, *13* (4), 335−339.
(45) Park, K.; Drummy, L. F.; Wadams, R. C.; Koerner, H.; Nepal, D.; Fabris, L.; Vaia, R. A. Growth Mechanism of Gold Nanorods. *Chem. Mater.* **2013**, *25* (4), 555−563.
(46) Hartland, G. V. Optical Studies of Dynamics in Noble Metal Nanostructures. *Chem. Rev.* **2011**, *111* (6), 3858−3887.
(47) Suits, A. G.; Continetti, R. E. *Imaging in Chemical Dynamics*; American Chemical Society: Washington, DC, 2001.
(48) Bormann, R.; Gulde, M.; Weismann, A.; Yalunin, S. V.; Ropers, C. Tip-Enhanced Strong-Field Photoemission. *Phys. Rev. Lett.* **2010**, *105* (14), 147601.
(49) Pettine, J.; Grubisic, A.; Nesbitt, D. J. Angle- and Momentum-Resolved Photoelectron Velocity Map Imaging Studies of Thin Au Film and Single Supported Au Nanoshells. *J. Phys. Chem. C* **2018**, *122* (7), 3970−3984.
(50) Berglund, C. N.; Spicer, W. E. Photoemission Studies of Copper and Silver: Theory. *Phys. Rev.* **1964**, *136* (4a), 1030−1044.
(51) Kanter, H. Slow-Electron Mean Free Paths in Aluminum, Silver, and Gold. *Phys. Rev. B* **1970**, *1* (2), 522−536.
(52) Ladstadter, F.; Hohenester, U.; Puschnig, P.; Ambrosch-Draxl, C. First-Principles Calculation of Hot-Electron Scattering in Metals. *Phys. Rev. B: Condens. Matter Mater. Phys.* **2004**, *70* (23), 235125.
(53) Chen, Q. Y.; Bates, C. W. Geometrical Factors in Enhanced Photoyield from Small Metal Particles. *Phys. Rev. Lett.* **1986**, *57* (21), 2737−2740.
(54) Blandre, E.; Jalas, D.; Petrov, A. Y.; Eich, M. Limit of Efficiency of Generation of Hot Electrons in Metals and Their Injection inside a Semiconductor using a Semiclassical Approach. *ACS Photonics* **2018**, *5* (9), 3613−3620.
(55) Ikhsanov, R. S.; Novitsky, A. V.; Protsenko, I. E.; Uskov, A. V. Bulk Photoemission from Plasmonic Nanoantennas of Different Shapes. *J. Phys. Chem. C* **2018**, *122* (22), 11985−11992.
(56) Jermyn, A. S.; Tagliabue, G.; Atwater, H. A.; Goddard, W. A.; Narang, P.; Sundararaman, R. Transport of Hot Carriers in Plasmonic Nanostructures. *Phys. Rev. Mater.* **2019**, *3* (7), 075201.
(57) Narang, P.; Sundararaman, R.; Jermyn, A. S.; Goddard, W. A.; Atwater, H. A. Cubic Nonlinearity Driven Up-Conversion in High-Field Plasmonic Hot Carrier Systems. *J. Phys. Chem. C* **2016**, *120* (37), 21056−21062.
(58) Stratton, J. A. *Electromagnetic Theory*, 1st ed.; McGraw-Hill, Inc.: New York, 1941.
(59) Merschdorf, M.; Pfeiffer, W.; Thon, A.; Voll, S.; Gerber, G. Photoemission from Multiply Excited Surface Plasmons in Ag Nanoparticles. *Appl. Phys. A: Mater. Sci. Process.* **2000**, *71* (5), 547−552.
(60) Grubisic, A.; Ringe, E.; Cobley, C. M.; Xia, Y. N.; Marks, L. D.; Van Duyne, R. P.; Nesbitt, D. J. Plasmonic Near-Electric Field Enhancement Effects in Ultrafast Photoelectron Emission: Correlated Spatial and Laser Polarization Microscopy Studies of Individual Ag Nanocubes. *Nano Lett.* **2012**, *12* (9), 4823−4829.
(61) Gong, Y.; Joly, A. G.; Hu, D.; El-Khoury, P. Z.; Hess, W. P. Ultrafast Imaging of Surface Plasmons Propagating on a Gold Surface. *Nano Lett.* **2015**, *15* (5), 3472−3478.
(62) Krüger, M.; Lemell, C.; Wachter, G.; Burgdörfer, J.; Hommelhoff, P. Attosecond Physics Phenomena at Nanometric Tips. *J. Phys. B: At., Mol. Opt. Phys.* **2018**, *51* (17), 172001.
(63) Fowler, R. H. The Analysis of Photoelectric Sensitivity Curves for Clean Metals at Various Temperatures. *Phys. Rev.* **1931**, *38* (1), 45−56.

https://dx.doi.org/10.1021/acsnano.0c09045
ACS Nano 2021, 15, 1566−1578

(64) Grajower, M.; Levy, U.; Khurgin, J. B. The Role of Surface Roughness in Plasmonic-Assisted Internal Photoemission Schottky Photodetectors. *ACS Photonics* **2018**, *5* (10), 4030−4036.
(65) Yalunin, S. V.; Gulde, M.; Ropers, C. Strong-Field Photoemission from Surfaces: Theoretical Approaches. *Phys. Rev. B: Condens. Matter Mater. Phys.* **2011**, *84* (19), 195426.
(66) Maier, S. A. *Plasmonics: Fundamentals and Applications*, 1st ed.; Springer: New York, 2007.
(67) Liao, P. F.; Wokaun, A. Lightning Rod Effect in Surface Enhanced Raman Scattering. *J. Chem. Phys.* **1982**, *76* (1), 751−752.
(68) Marsell, E.; Losquin, A.; Svard, R.; Miranda, M.; Guo, C.; Harth, A.; Lorek, E.; Mauritsson, J.; Arnold, C. L.; Xu, H. X.; L'Huillier, A.; Mikkelsen, A. Nanoscale Imaging of Local Few-Femtosecond Near-Field Dynamics within a Single Plasmonic Nanoantenna. *Nano Lett.* **2015**, *15* (10), 6601−6608.
(69) Hrelescu, C.; Sau, T. K.; Rogach, A. L.; Jäckel, F.; Laurent, G.; Douillard, L.; Charra, F. Selective Excitation of Individual Plasmonic Hotspots at the Tips of Single Gold Nanostars. *Nano Lett.* **2011**, *11* (2), 402−407.
(70) Lehr, M.; Bley, K.; Vogel, N.; Rethfeld, B.; Schönhense, G.; Elmers, H.-J. Evidence of Spatially Inhomogeneous Electron Temperature in a Resonantly Excited Array of Bow-Tie Nanoantennas. *J. Phys. Chem. C* **2019**, *123* (19), 12429−12436.
(71) Cherqui, C.; Thakkar, N.; Li, G. L.; Camden, J. P.; Masiello, D. J. Characterizing Localized Surface Plasmons Using Electron Energy-Loss Spectroscopy. *Annu. Rev. Phys. Chem.* **2016**, *67*, 331−357.
(72) Willets, K. A. Super-Resolution Imaging of SERS Hot Spots. *Chem. Soc. Rev.* **2014**, *43* (11), 3854−3864.
(73) Bhattarai, A.; El-Khoury, P. Z. Imaging Localized Electric Fields with Nanometer Precision through Tip-Enhanced Raman Scattering. *Chem. Commun.* **2017**, *53* (53), 7310−7313.
(74) Olmon, R. L.; Krenz, P. M.; Jones, A. C.; Boreman, G. D.; Raschke, M. B. Near-Field Imaging of Optical Antenna Modes in the Mid-Infrared. *Opt. Express* **2008**, *16* (25), 20295−20305.
(75) Kravtsov, V.; Ulbricht, R.; Atkin, J.; Raschke, M. B. Plasmonic Nanofocused Four-Wave Mixing for Femtosecond Near-Field Imaging. *Nat. Nanotechnol.* **2016**, *11* (5), 459−464.
(76) Perrault, S. D.; Chan, W. C. W. Synthesis and Surface Modification of Highly Monodispersed, Spherical Gold Nanoparticles of 50−200 nm. *J. Am. Chem. Soc.* **2009**, *131* (47), 17042−17043.
(77) Vigderman, L.; Zubarev, E. R. High-Yield Synthesis of Gold Nanorods with Longitudinal SPR Peak Greater than 1200 nm Using Hydroquinone as a Reducing Agent. *Chem. Mater.* **2013**, *25* (8), 1450−1457.
(78) Gonzalez-Rubio, G.; Kumar, V.; Llombart, P.; Diaz-Nunez, P.; Bladt, E.; Altantzis, T.; Bals, S.; Pena-Rodriguez, O.; Noya, E. G.; MacDowell, L. G.; Guerrero-Martinez, A.; Liz-Marzan, L. M. Disconnecting Symmetry Breaking from Seeded Growth for the Reproducible Synthesis of High Quality Gold Nanorods. *ACS Nano* **2019**, *13* (4), 4424−4435.
(79) Pettine, J.; Grubisic, A.; Nesbitt, D. J. Polarization-Controlled Directional Multiphoton Photoemission from Hot Spots on Single Au Nanoshells. *J. Phys. Chem. C* **2018**, *122* (26), 14805−14813.
(80) Johnson, P. B.; Christy, R. W. Optical Constants of Noble Metals. *Phys. Rev. B* **1972**, *6* (12), 4370−4379.

https://dx.doi.org/10.1021/acsnano.0c09045
ACS Nano 2021, 15, 1566−1578